PAN
ARCHIVES OF ACOUSTICS
Vol. **44**, No. 2, pp. 365–374 (2019)
DOI: 10.24425/aoa.2019.128500

Statistical Optimization of Underwater Lower-Frequency Sound Insulation for Locally Resonant Sonic Material Using Genetic Algorithm

Bo YUAN(1)*, Yong CHEN(2), Bilian TAN(3), Bo LI(1)

(1) *School of Mechanical Engineering*
Chongqing University of Technology
Chongqing, 400054, China
*Corresponding Author e-mail: ramboyuanbo@qq.com

(2) *College of Aerospace Science and Engineering*
National University of Defence Technology
Changsha, 410073, China

(3) *College of Arts and Science*
New York University
NY, 10012, USA

(*received November 10, 2017; accepted January 27, 2019*)

The locally resonant sonic material (LRSM) is an artificial metamaterial that can block underwater sound. The low-frequency insulation performance of LRSM can be enhanced by coupling local resonance and Bragg scattering effects. However, such method is hard to be experimentally proven as the best optimizing method. Hence, this paper proposes a statistical optimization method, which first finds a group of optimal solutions of an object function by utilizing genetic algorithm multiple times, and then analyzes the distribution of the fitness and the Euclidean distance of the obtained solutions, in order to verify whether the result is the global optimum. By using this method, we obtain the global optimal solution of the low-frequency insulation of LRSM. By varying parameters of the optimum, it can be found that the optimized insulation performance of the LRSM is contributed by the coupling of local resonance with Bragg scattering effect, as well as a distinct impedance mismatch between the matrix of LRSM and the surrounding water. This indicates coupling different effects with impedance mismatches is the best method to enhance the low-frequency insulation performance of LRSM.

Keywords: underwater acoustic; sound insulation; local resonance; statistical optimization; global optimum.

1. Introduction

Locally resonant sonic material (LRSM) is a type of artificial material with local resonators periodically embedded in a matrix. It can exhibit band gap characteristics when the wavelength of sound is still much larger than the material's periodicity, which is called "small size controlling long wavelengths" (Liu *et al.*, 2000). This type of artificial acoustic material attracted much attention from relevant fields of studies when it was first introduced; it has good prospects especially for low frequency sound absorption or insulation in underwater acoustics (Goffaux *et al.*, 2004; Zhao *et al.*, 2006; Wen *et al.*, 2011). Yet, since strong oscillation can only be stimulated when the frequency of sound is near the intrinsic frequency of local resonators, the band gap induced by local resonance inevitably has a deficiency of being too narrow. Hence, many studies have tried different ways to widen the band gap, such as designing new type of resonators (Jiang *et al.*, 2009; Elford *et al.*, 2011; Naify *et al.*, 2012; Varanasi *et al.*, 2013; Yu *et al.*, 2017), arranging different periodic patterns (Kuang *et al.*, 2006), coupling different band gaps (Xiao *et al.*, 2011; Yuan *et al.*, 2013), or optimizing components' parameters (Sigmund, Jensen, 2003; Meng *et al.*, 2012).

Yuan *et al.* (2013) analyzed the coupling behaviors of local resonance and Bragg scattering effects, and in-

dicated that the sound blocking performance of LRSM can be enhanced in both magnitude and bandwidth during coupling. Nonetheless, this analytical research lacks experimental proof that coupling different band gaps is the best strategy for improving sound insulation of LRSM, since it's impractical to fabricate and to test a vast amount of such artificial material with different properties. An alternative way is to analyze the optimal sound insulations of LRSM, which are obtained by the collaboration of optimization algorithm with numerical calculations. And if the optimal sound insulation of LRSM is just induced by the coupling of local resonance and Bragg scattering effects, then this insulation enhancing strategy will be proven valid.

To prove this hypothesis, the low-frequency sound blocking performance of an LRSM with 4 layers of spherical local resonators (LRs) is investigated by using statistical optimization. This LRSM is surrounded by water on both sides with plane waves perpendicularly incoming from the left side, as seen in Fig. 1.

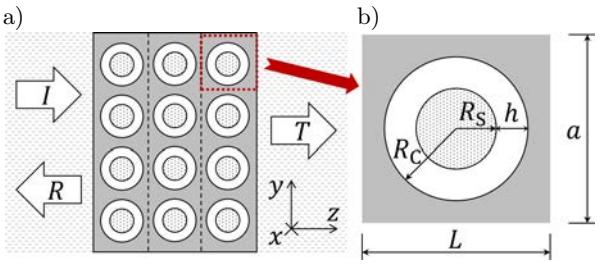

Fig. 1. A section view (a) of an LRSM with 4 layers of spherical local resonators (LRs), and the partial enlarged detail of one resonator (b). The dotted filling circles represent the cores of LRs, whose radius is R_S; the white thin annuli around the cores represent their coats, with the outer radius to be R_C, and the thickness of the coat to be h; the grey background represents the matrix; the dashed lines inside the matrix indicate the boundaries of different layers of LRs. Such a composite is periodically arranged in all three principle directions. It consists of finite layers of LRs in z-direction with the thickness of each layer to be L, but infinite rows and columns of LRs in x- and y-directions with the lattice constant to be a. The composite is immersed in water with plane waves normally incident on its left boundary.

There are many studies on the optimization algorithm for improving the performance of LRSM, such as simulated annealing, neighborhood algorithm, and Genetic Algorithm (GA) (Gothall, Westin, 2005). GA is highly adaptive to nonlinear, non-derivative, and multi-objective optimizations; thus it is suitable for improving the sound absorption and insulation of LRSM (Gazonas *et al.*, 2006; Romero-García *et al.*, 2009). Such method has been confirmed as a global optimization algorithm (Hartl, 1989). However, in regards to different optimizing objects and the coverage of initial populations, GA still has a chance to converge into a local minimum.

Consequently, this paper proposes to optimize the sound blocking performance of LRSM by invoking GA multiple times, and statistically analyze the solution set of multi-optimizations, in order to judge the globality of these optima. Since the multi-optimization will substantially increase the solving duration, such statistical analysis is rarely seen in GA applications (Yue, Feng, 2009). Yet, since this article calculates the acoustic behavior of LRSM by the Layer Multiple Scattering Theory (LMST) (Sainidou *et al.*, 2005), whose single calculation could be as short as a few seconds, it's achievable to obtain the global optimal solution of LRSM's sound blocking performance by multi-optimization, and thus to verify that the band gap coupling is the best strategy for sound insulation. The flow-process diagram for such statistical optimization is shown in Fig. 2.

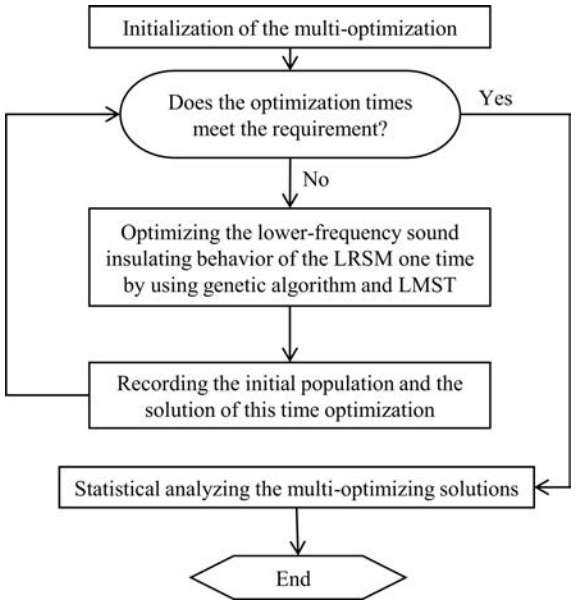

Fig. 2. The flow-process diagram for the statistical optimization using GA.

2. Statistical analysis of the optima's globality for multiple optimizations using Genetic Algorithm

The following content uses two functions to explain how to determine the global property of the optimal solutions through statistical analysis of multi-optimization. The two functions are Square-sum and Rastrigin, respectively, as shown below.

$$\text{Square-sum function:} \quad f(x,y) = x^2 + y^2, \tag{1}$$

$$\text{Rastrigin function:} \quad f(x,y) = x^2 + y^2 + 20 - 10\left(\cos 2\pi x + \cos 2\pi y\right). \tag{2}$$

Figure 3 shows the 3D surface graph and 2D contour graph of both functions in the solution space.

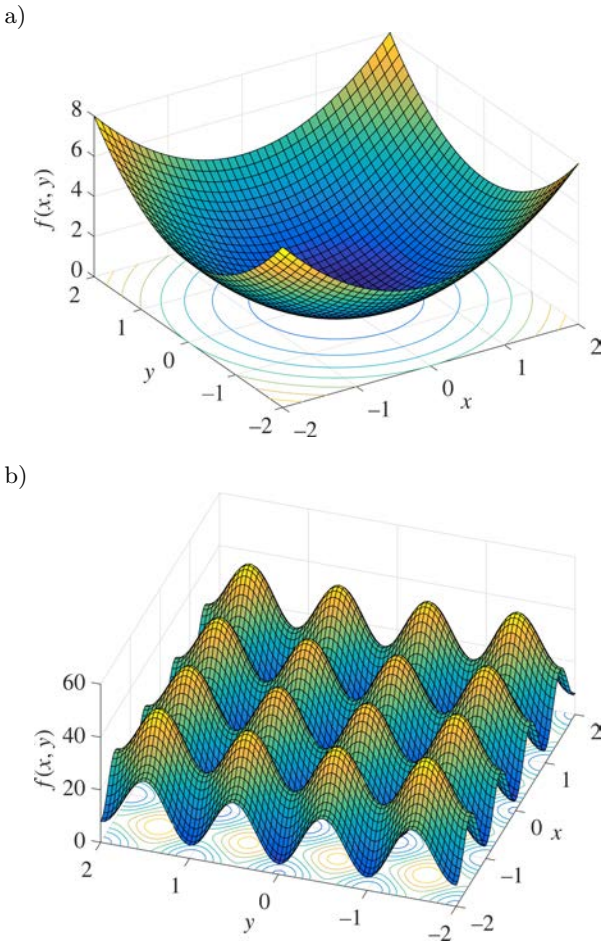

Fig. 3. 3D surface graph for Square-sum function (a) and Rastrigin function (b).

Each of the two functions has its own real variables (x and y), with range $[-2, 2]$. The difference is that Square-sum function contains only one minimal basin of attraction in the solution space, while Rastrigin function contains multiple minima with the global one at $x = 0$ and $y = 0$.

Figure 4a exhibits the scatter diagram of all initial populations from multiple optimizations, and the histogram for different variables of these initial points. These initial points together are named as the **initial population cluster**. Both the histogram and the scatter diagram in Fig. 4a show that the initial population cluster can evenly cover the entire solution space, which guarantees the GA to get the global optimal solution from different object functions. However, for Rastrigin function, which contains several global and local minima within one solution space, the initial population of a single optimization (shown as asterisks in Fig. 4a) may only cover parts of its attracting basins. To ensure at least one global optimum can be sought from multi-optimizations using GA, each object function will be optimized 1000 times, while 20 individuals will be contained in the initial population for each optimization.

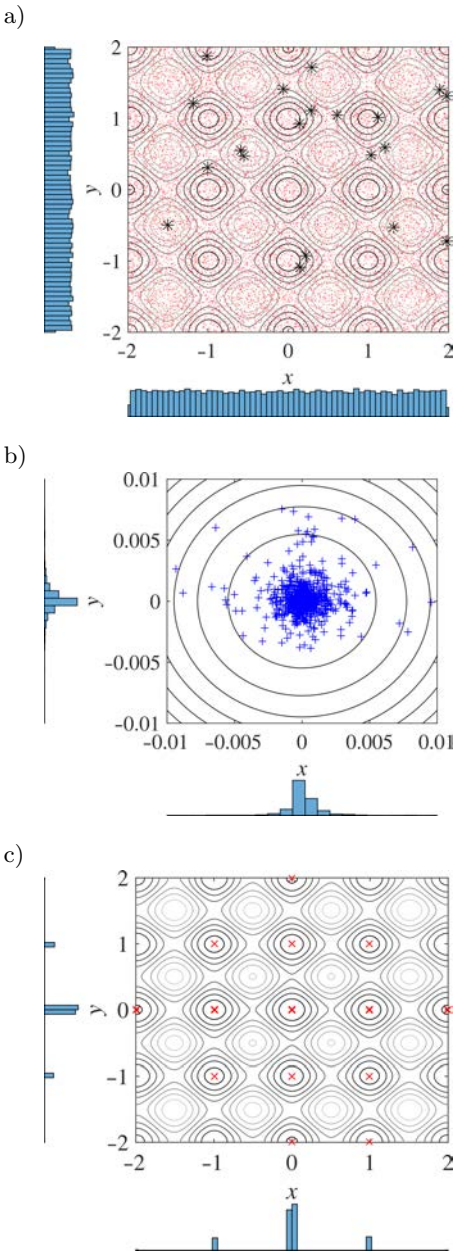

Fig. 4. The scatter diagram and histogram for the initial population cluster (a), the optimal solution set of Square-sum function (b) and those of Rastrigin function (c). Horizontal and vertical axes of scatter diagrams represent variables x and y respectively, while histograms aside from scatter diagrams represent the distribution of optimal solutions against corresponding variables. The red dots in (a) indicate all the points of the initial population cluster for multi-optimization, while black asterisks represent the initial population distribution for a single optimization; the blue plus marks in (b) are the optimal solution set for Square-sum; the red cross marks in (c) represent the optimal solution set for Rastrigin; the solid lines with different gray levels in scatter diagrams are the contour maps for either Square-sum (b) or Rastrigin (a, c) functions.

Figure 4b displays the scatter diagram of the optimal solutions for Square-sum function. After 1000

times of optimizations, the majority of the optimal solutions lies around the position of the function's global minimum ($x = 0$, $y = 0$). The distribution of these optima regards to each variable conforms to the normal distribution. As for Rastrigin function, the optimal solutions from multi-optimizations can not only converge to global minima but also to local ones, which can be observed from the scatter diagram in Fig. 4c. Nevertheless, the global optimum still has the highest occurrence probability.

Due to the fact that, distance among minima from different attracting basins, is much larger than those from the same attracting basin, the optimal solution set apparently exhibits discrete distribution against both variables (x or y).

There are two reasons the global optimum can be judged from the above analysis. The first one is that each of the two functions has only two variables, so the distance between the different optimal solutions can be observed directly on the scatter diagram. The second reason is that the global and local minima of both functions are already known before optimization. However, for realistic optimizing problems, an object function usually contains more than three variables, and nobody knows the real position of the global optimum in advance. Hence, this article tries to distinguish the globality of optimal solutions from multi-optimizations by analyzing their Fitness Value (FV) and **Euclidean Distance** (ED). The Euclidean distance is the normalized distance between each individual optimum and the average position of the optimal solution set, whose equation is shown as below:

$$\mathrm{ED}(X_i) = \sqrt{\sum_{k=1}^{m} \left(\frac{x_{ik} - \overline{x}_k}{\Delta x_k} \right)^2}, \tag{3}$$

where X_i is a gene for any individual from either the initial population cluster or the optimized solution set, which contains m variables like $X_i = (x_{i1}, x_{i2}, \cdots, x_{im})$, x_{ik} represents the k-th variables in i-th individual. For above functions, $X_i = (x_i, y_i)$. $\overline{x}_k$ is the arithmetic mean value for the k-th variable of all the individuals, while Δx_k is the span of k-th variable during the optimization (the distance between upper and lower bounds). The usage of Δx_k is to normalize the variation of each variable before calculating the Euclidean distance.

Figure 5 exhibits the distribution of fitness value and Euclidean distance of Square-sum function before and after multi-optimizations. By comparing histograms (a) and (c), one can find that fitness values of optimal solutions are much smaller than those of initial populations (by 6 orders of magnitude), which implies that the optimization does work. Since genetic algorithm is a stochastic optimization method, which generates slightly different optimal result each time, the optimal solutions by multi-optimizations are

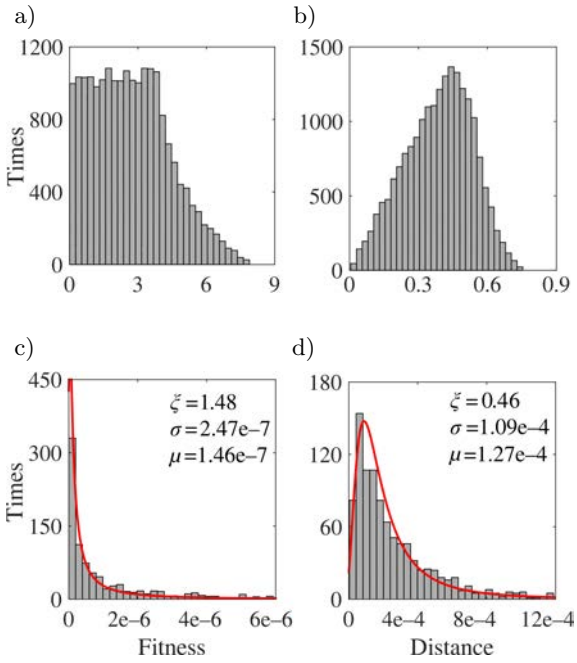

Fig. 5. The histograms of fitness value for Square-sum function before (a) and after (c) the statistical optimization, and their counterparts of Euclidean distance before (b) and after (d). The red solid lines in (c) and (d) represent the probability density curves of generalized extreme value (GEV) distribution fitted by the maximum likelihood method, whose specific parameters with 0.05 confidence level are noted on the upper-right corner of corresponding subfigure.

distributed continuously near the global minimum of Square-sum ($f_{\min} = 0$). It needs to be noted that the amount of individuals for initial population cluster is different from those for optimal solution set, in which the former has 20000 while the latter has 1000.

In addition, from Fig. 5b and d, it can be observed that the distances of the optimal solutions are also less than those of the initial population (by 3 orders of magnitude). This means that the optimal solution set has a good convergence in the solution space. Comparing with the fitness distribution, Euclidean distances of optimal solutions are also close to zero, and they too distribute continuously. However, the highest probability of occurrence is around 1.09e–4. Such distribution comes from the randomness of GA, causing each optimization to generate a slightly different result. Thus, most of optimal solutions locate around the center of the optimal solution set, while very few of them coincide.

Using maximum likelihood method, we tried to fit the fitness value and Euclidean distance of optimal solutions with different distribution patterns. Both of them can well match with the generalized extreme value (GEV) distribution, shown as red solid lines in Fig. 5c and 5d. The generalized extreme value distribution is used to model the smallest or largest value

among a large set of independently and identically distributed random values representing measurements or observations. If we treat all the generations of one GA optimization as a sample group, then the optimal solution of this optimization can be regarded as the minimum value of such sample group. Therefore, the optimal solutions from multi-optimizations should also satisfy the generalized extreme value distribution, whose probability density function is written as below:

$$f(z|\xi,\sigma,\mu) = \frac{1}{\sigma}\exp\left\{-\left[1+\frac{\xi(z-\mu)}{\sigma}\right]^{-\frac{1}{\xi}}\right\} \cdot \left[1+\frac{\xi(z-\mu)}{\sigma}\right]^{-1-\frac{1}{\xi}}. \quad (4)$$

Parameters ξ, σ and μ represent the shape, scale, and position of the probability density curve, respectively. We can estimate these parameters using maximum fitting method, but in regards to different optimizing problems, these parameters would also be different.

In contrast to Square-sum, the distribution of optimal solutions for Rastrigin apparently exhibits discrete pattern. As shown Fig. 6a, out of 1000 optimizations, there are 580 optimal solutions whose fitness values converge to zero (the global optimal solution at $x = 0$, $y = 0$), with 340 solutions converging to one, and several solutions converging to two and four. But for each discrete converging fitness values, the distribution of optimal solutions around it still obeys to GEV pattern. For instance, Fig. 6c shows the partial enlargement of the fitness distribution for optimal solutions around global optimum. By using maximum likelihood method, it can be found that the distribution of fitness matches the GEV's probability density curves well, whose specific parameters estimated under 0.05 confidence level are listed on the up-right of Fig. 6c.

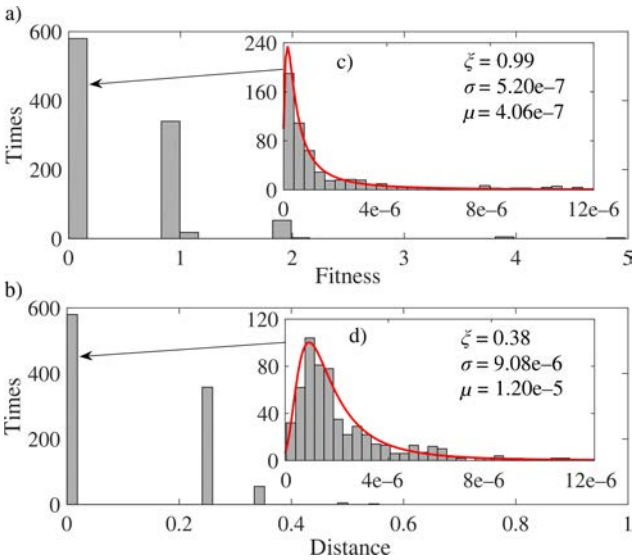

Fig. 6. Histograms of fitness value (a) and Euclidean distance (b) for optimal solutions of Rastrigin, and the partial enlargement distribution of fitness (c) and distance (d) around the global optimum ($x = 0$, $y = 0$). The meanings of red curves and parameters are the same with Fig. 4.

Hence, one way to distinguish the global optimal solution is to see whether the fitness distribution of optimal solutions belongs to a single minimum with continuous distribution, or several different minima with apparently discrete distribution; the latter indicates that these solutions contain local optima.

Nevertheless, judging the global optimum solely through the distribution of fitness value is not fully reliable. When the difference between the global optimum and local optima is small, their distributions may overlap each other, making it behave continuously like just one optimum. Such misjudgment can be averted by analyzing the distance distribution of optimal solutions simultaneously with fitness. When there are several optimal solutions from multi-optimization converging to local optima, they will locate in different attracting basins compared to the global optimum. No matter how close these different attracting basins are, and how similar their fitness value are, the distance of optimal solutions from one basin will be much smaller than those from different basins. So, the distance of optimal solutions will distribute discretely, if only they are converged to different optima.

Figure 6b shows the distribution of Euclidean distance of optimal solution set for Rastrigin, which shows apparent discrete pattern. Most of the distances concentrate on the value of 0 and 0.25, while others on 0.35 and 0.5. Those results whose distance are close to 0 are the optimal solutions converged to global minimum, while others converged to different local minima. By referring Fig. 3c and Eq. (2), it can be observed that distance values of 0.25 and 0.35 represent the optimal solutions which converges to local minima at positions of $(\pm 1, 0)$ and $(\pm 1, \pm 1)$ respectively. That means the discrete distance of multi-optimization coincides with the distance from local minima at the center. For the partially enlargement distribution around any specific discrete distance, it matches with the GEV distribution under 0.05 confidence level, which is shown in Fig. 6d.

According to the above analysis, we can derive the **global optimum criterion** of the statistical optimization: if the fitness value and Euclidean distance of the optimal solution set distribute continuously in their own value range, and their patterns match with the generalized extreme value distribution, it would mean the optimal solution set converge to the global optimum. Otherwise, if the fitness value or Euclidean distance distribute discretely, it means there are solutions converged to local minima during multiple optimizations.

3. LRSM sound insulation statistical optimization verification

Yuan *et al.* (2013) proposed enhancing the sound blocking performance of LRSM by coupling local resonance and Bragg scattering effect. To prove this hypothesis, the following optimization used the LRSM structure mentioned in the introduction section as reference, as shown in Fig. 1. The optimizing variables and their boundaries of such 4 layers LRSM are listed in Table 1. L is the layer thickness of LRs in z-direction, R_{S} is the core's radius, R_{C} is the outer radius of coat, ρ_{M}, E_{M}, σ_{M} are the density, Young's modulus, and Poisson's ratio of the matrix, respectively; ρ_{C}, E_{C}, σ_{C} are the corresponding material properties of the coat, and ρ_{S} is the core's density. In addition, the cell's lattice constant is $a = 10$ mm. For easier recognition of the sound blocking effect induced by gap coupling, the material's damping is not considered during optimization.

Since the optimizing goal is improving the low-frequency sound blocking performance of LRSM, the object function should try to maximize the average value of transmission loss ($TL = 10\lg {}^{1}\!/\!_{T}$) of the LRSM on the weight mean of low-frequency in considered frequency range. For a genetic algorithm which tries to minimize the fitness of individuals, the specific form of the estimating function of fitness is shown as follow:

$$F(X_i) = \frac{\sum_{j=1}^{n} 10 \cdot \dfrac{\Delta\omega^2}{\omega_j^2} \cdot \lg T\left(X_i, \omega_j\right)}{n}, \tag{5}$$

where X_i is the i-th individual for estimating fitness; ω_j is the j-th discrete frequency for calculating the sound transmission (T) of the LRSM, while there are n points of discrete frequencies which needs to be calculated in considered frequency range; $\Delta\omega$ is the considered frequency range for the optimization ($\Delta\omega = \omega_n - \omega_1$), which is set as $f \in [500, 2500]$ in this paper. $\Delta\omega^2/\omega_j^2$ is the weight factor which considers the low-frequency sound blocking performance to be more important than that of the relatively high-frequency. The sound transmission (T) in regards to different frequencies is calculated by the Layer Multiple Scattering Theory (LMST) according to the X_i individual (Sainidou *et al.*, 2005).

Ignoring the time domain term $\exp(i\omega t)$, an incident wave is normally represented as:

$$\mathbf{u}_{\mathrm{in}}(\mathbf{r}) = \left[u_{\mathrm{in}}\right]^{s'}_{\mathbf{g}'i'} \exp\left(-i\mathbf{K}^{s'}_{\mathbf{g}'i'} \cdot \mathbf{r}\right) \widehat{\mathbf{e}}_{i'}\left(\mathbf{K}^{s'}_{\mathbf{g}'i'}\right), \tag{6}$$

in which, $\mathbf{g}'$ implies the reciprocal lattice vector of the structure, $i' = 1, 2, 3$ represents the longitudinal wave and two transverse waves respectively, $s' = \pm$ indicates the wave going through $+z$ or $-z$ directions, and $\mathbf{K}^{s'}_{\mathbf{g}'i'}$ implies the wave vector:

$$\mathbf{K}^{\pm}_{\mathbf{g}'i'} = \left(\mathbf{k}_{//} + \mathbf{g}' \pm \sqrt{q_{i'}^2 - \left|\mathbf{k}_{//} + \mathbf{g}'\right|^2}\right). \tag{7}$$

q_1 represents the longitudinal wave number, while q_2 and q_3 represent the wave number of two transverse waves; $\mathbf{k}_{//}$ is the reduced Bloch vector which lies in the xy plane; $\left[u_{\mathrm{in}}\right]^{s'}_{\mathbf{g}'i'}$ indicates the amplitude of incident wave; $\widehat{\mathbf{e}}_{i'}(\mathbf{K}^{s'}_{\mathbf{g}'i'})$ is the unit vector with corresponding polarization. Hence, the incident wave (Eq. (6)) can be derived as:

$$\mathbf{u}_{\mathrm{in}}(\mathbf{r}) = \sum_{n\sigma} a^{\mathrm{in}}_{n\sigma} \mathbf{J}_{n\sigma}(\mathbf{r}). \tag{8}$$

The scattering wave of the one layer periodicity structure, when the wave given by Eq. (8) is incident upon it, has the form

$$\mathbf{u}_{sc}(\mathbf{r}) = \sum_{n\sigma} b^0_{n\sigma} \sum_j \exp\left(-i\mathbf{k}_{//} \cdot \mathbf{R}_j\right) \mathbf{H}_{n\sigma}(\mathbf{r} - \mathbf{R}_j), \tag{9}$$

where $\mathbf{R}_j$ is the position vector of the scatter, $\mathbf{J}_{n\sigma}(\mathbf{r})$ and $\mathbf{H}_{n\sigma}(\mathbf{r})$ are vector spherical wave function.

Since the total incident waves of the scatter at original position are equal to the summation of incident wave from the outside environment and the scattering waves from all other scatters, the following equation can be obtained as:

$$\begin{aligned} \mathbf{u}^0_{\mathrm{in}}(\mathbf{r}) &= \sum_{n\sigma} a^0_{n\sigma} \mathbf{J}_{n\sigma}(\mathbf{r}) \\ &= \sum_{n\sigma} \left(a^{\mathrm{in}}_{n\sigma} + \sum_{n'\varrho'} \Omega_{n\sigma n'\sigma'}\left(\mathbf{k}_{//}\right) b^0_{n'\sigma'} \right) \mathbf{J}_{n\sigma}(\mathbf{r}), \end{aligned} \tag{10}$$

where

$$\Omega_{n\sigma n'\sigma'}\left(\mathbf{k}_{//}\right) = \sum_{j\neq 0} \exp\left(-i\mathbf{k}_{//} \cdot \mathbf{R}_j\right) G_{n'\sigma' n\sigma}(-\mathbf{R}_j),$$

and $G_{n'\sigma' n\sigma}$ is the constant structure vector for the periodic arranged scatters. On the other hand, the scattering and incidence coefficients of one scatter satisfy the following relationship:

$$b^0_{n\sigma} = \sum_{n'\sigma'} T_{n\sigma n'\sigma'} a^0_{n'\sigma'}, \tag{11}$$

Table 1. The optimizing variables and their boundaries of the LRSM with 4 layers of spherical LRs.

Variables	L	R_{S}	R_{C}	ρ_{M}	E_{M}	σ_{M}	ρ_{C}	E_{C}	σ_{C}	ρ_{S}
Lower bound	10	0.01	0.5	800	1e6	0.30	800	1e5	0.2	2600
Upper bound	20	4.5	5	1300	1e9	0.497	1300	1e7	0.497	11600

Note: unit of L, R_{S} and R_{C} is mm, unit of ρ_{M}, ρ_{C}, and ρ_{S} is kg/m^3, unit of E_{M} and E_{C} is Pa.

where $T_{n\sigma n'\sigma'}$ represents the transfer matrix of the scatter. By combining Eqs (10) and (11), we can derive the $b^0_{n\sigma}$, and the scattered wave of the whole layer of scatters as follows:

$$\mathbf{u}_{\mathrm{sc}}(\mathbf{r}) = \sum_{\mathbf{g}i} [u_{\mathrm{sc}}]^s_{\mathbf{g}i} \exp\left(-i\mathbf{K}^{s'}_{\mathbf{g}'i'} \cdot \mathbf{r}\right) \widehat{\mathbf{e}}_i\left(\mathbf{K}^s_{\mathbf{g}i}\right). \quad (12)$$

Thus, the reflected and transmitted waves of this layer are represented as:

$$\begin{aligned} \mathbf{u}_{\mathrm{rf}}(\mathbf{r}) &= \sum_{\mathbf{g}i} [u_{\mathrm{rf}}]_{\mathbf{g}i} \exp\left(-i\mathbf{K}^-_{\mathbf{g}i} \cdot \mathbf{r}\right) \widehat{\mathbf{e}}_i\left(\mathbf{K}^-_{\mathbf{g}i}\right), \\ \mathbf{u}_{\mathrm{tr}}(\mathbf{r}) &= \sum_{\mathbf{g}i} [u_{\mathrm{tr}}]^s_{\mathbf{g}i} \exp\left(-i\mathbf{K}^+_{\mathbf{g}i} \cdot \mathbf{r}\right) \widehat{\mathbf{e}}_i\left(\mathbf{K}^+_{\mathbf{g}i}\right). \end{aligned} \quad (13)$$

The coefficient of reflected and transmitted waves for the n-th layer of scatters ($[u_{\mathrm{rf}}]_{\mathbf{g}i}$ and $[u_{\mathrm{tr}}]_{\mathbf{g}i}$) are linearly related with its incident coefficient $[u_{\mathrm{in}}]^+_{\mathbf{g}'i'}$. Such relationship can be defined as forward transmission (Q^{I}) and reflection (Q^{III}) matrices for a plane wave incident from left. On the contrary, Q^{IV} and Q^{II} represents the inverse transmission and reflection matrices when the incident wave comes from right side $[u_{\mathrm{in}}]^-_{\mathbf{g}'i'}$. The physical meaning of these matrices are shown schematically in Fig. 7.

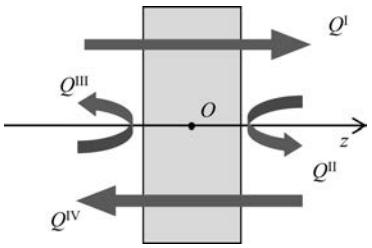

Fig. 7. The physical meaning of Q^k.

We can obtain the scattering matrices Q^k for any kinds of multiple layers with different periodic spherical scatters or homogenous planes, by successively calculating all the scattering matrices for each layer. The transmission and reflection matrices for a pair of two successive layers, n and $n+1$, to be denoted by $Q^k(n, n+1)$, can be obtained by combining the matrices $Q^k(n)$ and $Q^k(n+1)$ of the two layers as follows:

$$\begin{aligned} Q^{\mathrm{I}}(n,n+1) &= Q^{\mathrm{I}}(n+1) \\ &\quad \cdot \left[I - Q^{\mathrm{II}}(n)Q^{\mathrm{III}}(n+1)\right]^{-1} Q^{\mathrm{I}}(n), \\ Q^{\mathrm{II}}(n,n+1) &= Q^{\mathrm{II}}(n+1) + Q^{\mathrm{I}}(n+1)Q^{\mathrm{II}}(n) \\ &\quad \cdot \left[I - Q^{\mathrm{III}}(n+1)Q^{\mathrm{II}}(n)\right]^{-1} Q^{\mathrm{IV}}(n+1), \\ Q^{\mathrm{III}}(n,n+1) &= Q^{\mathrm{III}}(n) + Q^{\mathrm{IV}}(n)Q^{\mathrm{III}}(n+1) \\ &\quad \cdot \left[I - Q^{\mathrm{II}}(n+1)Q^{\mathrm{III}}(n+1)\right]^{-1} Q^{\mathrm{I}}(n), \\ Q^{\mathrm{IV}}(n,n+1) &= Q^{\mathrm{IV}}(n) \\ &\quad \cdot \left[I - Q^{\mathrm{III}}(n+1)Q^{\mathrm{II}}(n)\right]^{-1} Q^{\mathrm{IV}}(n+1). \end{aligned} \quad (14)$$

Hence, we can analytically calculate the sound performance of a locally resonant sonic material with multiple layers by using Eq. (14). Finally, the transmittance and reflectance of the acoustic material can be calculated as follows:

$$T = \frac{\sum_{\mathbf{g}i} \rho^{\mathrm{tr}} (c_i^{\mathrm{tr}})^2 [u_{\mathrm{tr}}]_{\mathbf{g}i} ([u_{\mathrm{tr}}]_{\mathbf{g}i})^* K^{+(\mathrm{tr})}_{\mathbf{g}iz}}{\sum_{\mathbf{g}i} \rho^{\mathrm{in}} (c_i^{\mathrm{in}})^2 [u_{\mathrm{in}}]_{\mathbf{g}i} ([u_{\mathrm{in}}]_{\mathbf{g}i})^* K^{+(\mathrm{in})}_{\mathbf{g}iz}}, \quad (15)$$

$$R = \frac{\sum_{\mathbf{g}i} (c_i^{\mathrm{in}})^2 [u_{\mathrm{rf}}]_{\mathbf{g}i} ([u_{\mathrm{rf}}]_{\mathbf{g}i})^* K^{+(\mathrm{in})}_{\mathbf{g}iz}}{\sum_{\mathbf{g}i} (c_i^{\mathrm{in}})^2 [u_{\mathrm{in}}]_{\mathbf{g}i} ([u_{\mathrm{in}}]_{\mathbf{g}i})^* K^{+(\mathrm{in})}_{\mathbf{g}iz}}. \quad (16)$$

If absorption is present in any components of the acoustic material, we can obtain the absorbance A of such material

$$A = 1 - T - R. \quad (17)$$

Figure 8 is the cluster of transmission loss (TL) curves of the LRSM optimized by statistical optimization 100 times. It can be seen that all optimal solutions exhibit high-efficient sound insulation in the range of 350–1800 Hz, with the average transmission loss up to 78 dB and the peak up to 200 dB. According to shapes of these curves, it can be preliminarily judged that the high-efficient sound blocking band is induced by the coupling of local resonance and Bragg scattering effect (Yuan *et al.*, 2013). There are three TL peaks whose peaks are up to 20 dB in the range of 0–350 Hz for all optimal solutions, and their shapes are highly uniform. They are induced by the Fabry-Pérot interference on the boundaries of the LRSM. Since the characteristic impedance of LRSM's matrix is seriously mismatched with the surrounding water, the acoustic material can still insulate the incoming sound efficiently even in the frequency range of pass band (for its counterpart with

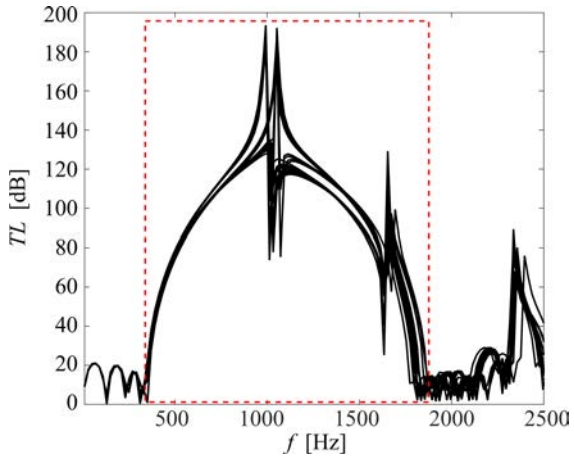

Fig. 8. The cluster of transmission loss (TL) curves of the LRSM optimized by statistical optimization 100 times.

infinite layers in z-direction, which is named as locally resonant phononic crystal). This indicates that reducing the matrix's impedance, thus increasing the impedance imbalance between matrix and surrounding will enhance the sound insulation performance of the material. In addition, optimal solutions also exhibit several sound blocking peak when frequency is higher than 1800 Hz, which are caused by different reasons like impedance imbalance, higher mode of local resonance, and surface localized mode (Sainidou *et al.*, 2008).

Although, there are slight differences on the frequency ranges or curve shapes for different optimal solutions, their basic trends of the transmission loss curves are the same, which means the sound blocking characteristic of these optimal solutions has high consistency. Therefore, it can be preliminarily concluded these optimal solutions has converged to the global optimum.

Figure 9 shows fitness and distance distributions for the initial population cluster and the optimal solution set respectively. As shown in Fig. 9a and 9b, most fitness values of the initial population cluster are close to 0, while all of optimal solutions are below −500. Such value distribution indicates that the initial population has no apparent sound insulation, while their optimizing results exhibit efficient insulation in low frequency range. Besides, the Euclidean distances of initial populations are far greater than those of optimized results, which implies the optimal solutions obtained by multi-optimization has a good convergence in the solution space. The statements above can prove that using Eq. (5) as objective function has indeed optimized the low-frequency sound insulation performance of LRSM.

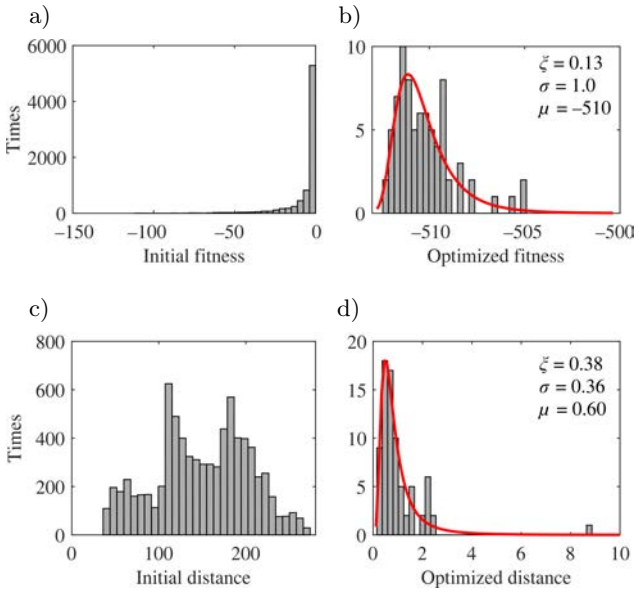

Fig. 9. The fitness and distance distribution of initial populations and optimal solutions for sound blocking optimization of LRSM.

By using the maximum likelihood method, we try to fit the distribution of fitness and distance of optimal solutions with GEV distribution, which are shown as solid curves in Fig. 9b and 9d. The corresponding parameters (ξ, σ, and μ) of GEV are noted on the upright of subfigures respectively with the confident level at $\alpha = 0.05$. It can be found that both fitness and distance of the optimal solutions fit the GEV distribution well, and behave continuously in their value range. According to the global optimum criterion in last section, we can confirm the optimal solutions of low-frequency sound blocking performance have converged to the global optimum in the given variation space.

The specific parameters of the best solution from multi-optimization are shown in Table 2. In order to enhance the low-frequency sound blocking performance of the LRSM, the optimization converged to a relatively large radius and heavy density core, while a low Young's modulus and thick coat, compared with the boundaries of variables in Table 1. This can reduce the resonant frequency of local resonators. Simultaneously, the optimized matrix has relatively slow longitudinal and transverse waves, and large layer thickness, so as to decrease the starting frequency of Bragg scattering effect.

Table 2. The specific parameters for the best optimal solution of LRSM.

Parameters/Components	Core	Coat	Matrix
Density ρ [kg/m^3]	11600	816	802
Young's modulus E [Pa]	4.08e10	1.00e5	1.01e6
Poisson ratio σ	0.37	0.21	0.30
Longitudinal speed c_{L} [m/s]	2493	11.72	41.16
Transverse speed c_{S} [m/s]	1133	9.13	21.94
Structural size [mm]	$R_{\mathrm{S}} = 4.5$	$R_{\mathrm{C}} = 5$	$a = 10$ $L = 20$

Figure 10 shows the transmission loss spectrum of the best solution from multi-optimization, and its derived cases. The best solution ($E_{\mathrm{C}} = 0.1$ MPa) exhibits an unified and efficient sound blocking band in the range of 350–1800 Hz, and contains two peaks at 1013 Hz and 1657 Hz, respectively. When the Young's modulus of the LR's coat is reduced to the half of the best optimal solution ($E_{\mathrm{C}} = 0.05$ MPa), the derived case exhibits two apparent sound blocking band in the range of 300–1600 Hz. The curve of the band in lower frequency range has a cusp at 616 Hz where the peak of transmission loss reaches 200 dB, while the counterpart in higher frequency range varies smoothly in the range of 854–1600 Hz where the transmission loss never exceeds 100 dB (shown as the dashed curve in Fig. 9). On the other hand, when the Young's modulus of the LR's coat is twice of the best optimal solution ($E_{\mathrm{C}} = 0.2$ MPa), the derived case also exhibits

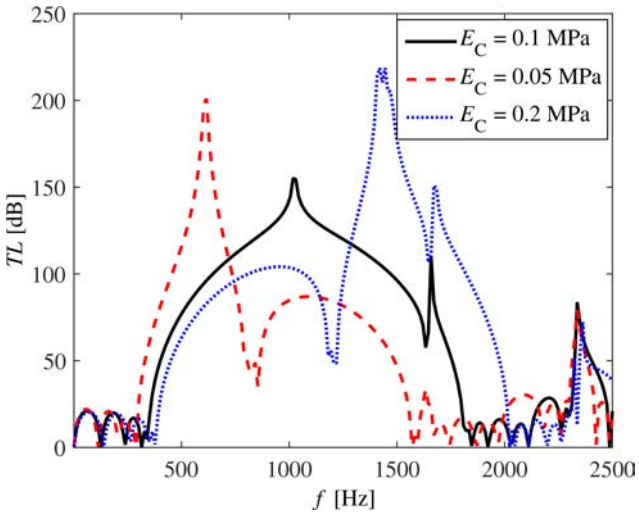

Fig. 10. The transmission loss spectrum of the best solution from multi-optimization (solid curve), and its derived cases (dashed and dotted curves).

two apparent sound blocking bands in the range of 400–2000 Hz. What's different with the former derived case is that the sound blocking band in lower frequency range varies smoothly, while the higher one has a cusp in the middle of the band (shown as the dotted curve in Fig. 10). Such varying pattern of sound blocking performance is coincident with the gap coupling characteristics discussed in (Yuan *et al.*, 2013), which implies the highly efficient sound blocking performance of the best optimal solution in low frequency range is induced by gap coupling of local resonance and Bragg scattering effects. In addition, two derived cases with uncoupled gaps (the dashed and dotted curves in Fig. 10) could be further designed as underwater wave filter with specific frequency range.

4. Conclusion

To prove the best strategy of enhancing the sound blocking performance of LRSM includes impedance imbalance as well as the gap coupling between local resonance and Bragg scattering, this article suggests using genetic algorithm to optimize the low-frequency insulation of LRSM, and analyze the formation of optimized sound insulation characteristic. Since there are a dozen of the LRSM's parameters needed to be optimized, one sole optimization may not be able to converge to the global optimum for the sound blocking performance. Thus, we utilize the genetic algorithm to optimize problems multiple times, and try to judge the globality of solutions with statistical analysis. The Square-sum and Rastrigin functions are used as examples to conclude the criterion of global optimum, which should be: the fitness values and Euclidean distance of the optimal solutions distribute continuously and match with the generalized extreme value distribution. By using such statistical optimization method, we obtain the global optimum of the LRSM for the best sound blocking performance in low-frequency, which exhibits highly efficient insulation in the frequency range of 350–1800 Hz with the average transmission loss up to 78 dB. Further investigation confirms such insulation performance is mainly induced by the impedance imbalance between the matrix and surrounding water, as well as the gap coupling between local resonance and Bragg scattering effects. This study reveals that by integrating impedance imbalance and gap coupling methods, one can substantially enhance the sound insulation of LRSM. What's more, the imperfect gap-coupling case has the potential to become underwater sound filtering material.

Acknowledgment

This research is funded by the National Natural Science Foundation of China under Grant Nos. 11504427, 11404405 and 51505494. Parts of the work are accomplished at the MOE Key Laboratory of Photonic and Phononic Crystals in National University of Defence Technology.

References

1. Elford D.P., Chalmers L., Kusmartsev F.V., Swallowe G.M. (2011), *Matryoshka locally resonant sonic crystal*, The Journal of the Acoustical Society of America, **130**, 5, 2746–2755.
2. Gazonas G.A., Weile D.S., Wildman R., Mohan A. (2006), *Genetic algorithm optimization of phononic bandgap structures*, International Journal of Solids and Structures, **43**, 18, 5851–5866.
3. Goffaux C., Sanchez-Dehesa J., Lambin P. (2004), *Comparison of the sound attenuation efficiency of locally resonant materials and elastic band-gap structures*, Physical Review B, **70**, 18, 184302, 6 pages, doi: 10.1103/PhysRevB.70.184302.
4. Gothall H., Westin R. (2005), *Evaluation of four global optimisation techniques (ASSA, DE, NA, Tabu Search) as applied to anechoic coating design and iverse problem uncertainty estimation*, Swedish Defence Research Agency, Stockholm.
5. Hartl R. (1989), *A global convergence proof for a class of genetic algorithms*, http://citeseerx.ist.psu.edu/viewdoc/summary?doi=10.1.1.330.1662.
6. Jiang H., Wang Y., Zhang M., Hu Y., Lan D., Zhang Y., Wei B. (2009), *Locally resonant phononic woodpile: A wide band anomalous underwater acoustic absorbing material*, Applied Physics Letters, **95**, 10, 104101.
7. Kuang W., Hou Z., Liu Y., Li H. (2006), *The band gaps of cubic phononic crystals with different shapes of scatterers*, Journal of Physics D: Applied Physics, **39**, 10, 2067.

8. Liu Z., Zhang X., Mao Y., Zhu Y.Y., Yang Z., Chan C.T., Sheng P. (2000), *Locally resonant sonic materials*, Science, **289**, 5485, 1734–1736.

9. Meng H., Wen J., Zhao H., Wen X. (2012), *Optimization of locally resonant acoustic metamaterials on underwater sound absorption characteristics*, Journal of Sound and Vibration, **331**, 20, 4406–4416.

10. Naify C.J., Chang C.-M., McKnight G., Nutt S.R. (2012), *Scaling of membrane-type locally resonant acoustic metamaterial arrays*, The Journal of the Acoustical Society of America, **132**, 4, 2784–2792.

11. Romero-García V., Sánchez-Pérez J.V., García-Raffi L.M., Herrero J.M., García-Nieto S., Blasco X. (2009), *Hole distribution in phononic crystals: Design and optimization*, The Journal of the Acoustical Society of America, **125**, 6, 3774–3783.

12. Sainidou R., Djafari-Rouhani B., Vasseur J.O. (2008), *Surface acoustic waves in finite slabs of three-dimensional phononic crystals*, Physical Review B, **77**, 9, 094304.

13. Sainidou R., Stefanou N., Psarobas I.E., Modinos A. (2005), *A layer-multiple-scattering method for phononic crystals and heterostructures of such*, Computer Physics Communications, **166**, 3, 197–240.

14. Sigmund O., Jensen J.S. (2003), *Systematic design of phononic band–gap materials and structures by topology optimization*, Philosophical Transactions of the Royal Society of London. Series A: Mathematical, Physical and Engineering Sciences, **361**, 1806, 1001–1019.

15. Varanasi S., Bolton J.S., Siegmund T.H., Cipra R.J. (2013), *The low frequency performance of metamaterial barriers based on cellular structures*, Applied Acoustics, **74**, 4, 485–495.

16. Wen J., Zhao H., Lv L., Yuan B., Wang G., Wen X. (2011), *Effects of locally resonant modes on underwater sound absorption in viscoelastic materials*, The Journal of the Acoustical Society of America, **130**, 3, 1201–1208.

17. Xiao Y., Mace B., Wen J., Wen X. (2011), *Formation and coupling of band gaps in a locally resonant elastic system comprising a string with attached resonators*, Physics Letters A, **375**, 1485–1491.

18. Yu X., Lu Z., Cheng L., Cui F. (2017), *On the sound insulation of acoustic metasurface using a substructuring*, Journal of Sound and Vibration, **401**, 190–203.

19. Yuan B., Humphrey V.F., Wen J., Wen X. (2013), *On the coupling of resonance and Bragg scattering effects in three-dimensional locally resonant sonic materials*, Ultrasonics, **53**, 7, 1332–1343.

20. Yue Q., Feng S. (2009), *The statistical analyses for computational performance of the genetic algorithms* [in Chinese], Chinese Journal of Computers, **32**, 12, 1–5.

21. Zhao H., Liu Y., Wen J., Yu D., Wang G., Wen X. (2006), *Sound absorption of locally resonant sonic materials*, Chinese Physics Letter, **23**, 8, 2132–2134.